EDGE ARTICLE

Check for updates

Coupling abundant active sites and an ultra-short ion diffusion path: R–VO₂/carbon nanotube composite microspheres boosted the performance of aqueous ammonium-ion batteries

Lin-bo Tang,†[ab] Xian-kai Fan,†[ac] Kai-xiong Xiang,[d] Wei Zhou,[a] Wei-na Deng, [iD] [a] Hai Zhu,[a] Liang Chen,[a] Jun-chao Zheng [iD] *[b] and Han Chen*[a]

Ammonium (NH_4^+) ions as charge carriers have exhibited tremendous potential in aqueous batteries because of their abundant resources, ultrafast reaction kinetics, and negligible dendrite risks. However, the choices of cathode materials have resulted in relatively low capacities in aqueous ammonium ion batteries (AAIBs). Herein, double tunnel NH_4^+ ion insertion behavior with hydrogen bond building-breaking in rutile-phase VO_2 (R–VO_2) microspheres was revealed for the first time, and the capacity contribution was confirmed to be dominated by surface-control according to kinetic analysis and density functional theory (DFT) calculations. Composite microspheres with R–VO_2 and carbon nanotubes (R–VO_2/CNTs) were acquired to comprehensively improve the capacity, rate performance, and cycling stability of R–VO_2 microspheres. In addition, R–VO_2/CNT composite microspheres exhibited excellent capacity (950 mAh g⁻¹) within −1.3−0.8 V at 0.05 A g⁻¹, which was maintained at 170 mAh g⁻¹ at 5 A g⁻¹, and achieved excellent capacity retention of 113% at the 5000th cycle and 0−0.4 V. To explore their practical application, a full cell was constructed by coupling a R–VO_2/CNT composite microsphere cathode with a urea-perylene diimide polymer (UP) anode. Excellent capacity (130 mAh g⁻¹) with imperceptible capacity decay following 2500 cycles at 1 A g⁻¹ was achieved within the 0−0.9 V practical voltage range. In summary, R–VO_2/CNT composite microspheres have been demonstrated for potential application in sustainable energy storage in AAIBs.

1. Introduction

Green renewable energy sources such as wind, solar, and tidal power represent popular strategies for alleviating the high burden of global warming resulting from excess carbon emission in the human and ecological environment, and for achieving net-zero carbon emission or carbon neutrality, whereas the extremely unbalanced space-time distribution of renewable energy sources inevitably increases the difficulty of their development and utilization.[1,2] Lithium-ion batteries, devices contributing to sustainable energy storage, are an effective solution to couple intermittent clean energy with intelligent grids because of their high energy density, excellent industrial applicability and technical maturity .[2,3] Nevertheless, the high cost, insufficient resources, and unsatisfactory security caused by thermal runaway and organic electrolytes for lithium-ion batteries are problems, representing urgent issues in the development of a new generation of energy storage devices.[4,5]

Aqueous ion batteries have exhibited great benefits and prominent applications in the field of energy storage because of their cost-effectiveness, inherent security, high ionic conductivity, and environmental friendliness.[6,7] Therefore, various metal carriers, such as Li^+,[8,9] Na^+,[10,11] K^+,[12] Mg^{2+},[13,14] Ca^{2+},[15] Zn^{2+},[16,17] and Al^{3+},[18] have been exploited in aqueous energy storage systems. Moreover, non-metal ammonium NH_4^+ ions are regarded to be charge carriers for aqueous battery chemistry. Like metal ion carriers, NH_4^+ ions comply with the working principles of the model, commuting back and forth between the cathode and anode within batteries.[19,20] Significantly, NH_4^+ ions display greater application potential in aqueous batteries than metal ions due to their abundant natural resources (nitrogen element and hydrogen element), lack of dendrite risk, ultrafast reaction kinetics benefiting from their low molar mass (18 g mol⁻¹), and the specific interaction (hydrogen bonding) of NH_4^+ ions with electrode hosts.[19,21]

[a]*School of Materials and Environmental Engineering, Changsha University, Changsha 410022, PR China. E-mail: lzdxnchh@126.com*

[b]*School of Metallurgy and Environment, Central South University, Changsha, Hunan, 410083, China. E-mail: jczheng@csu.edu.cn*

[c]*College of Energy Materials and Chemistry, Inner Mongolia University, Hohhot, Inner Mongolia, 011123, PR China*

[d]*Liling Ceramic Institute, Hunan University of Technology, Zhuzhou, Hunan, 412007, PR China*

† Lin-bo Tang and Xian-kai Fan contributed equally to this study.

The cathode materials for AAIBs represent one of the pivotal factors that determine the electrochemical performance and have attracted considerable attention over the past decade. Prussian blue analog (PBA) materials used in $K_{0.9}Cu_{1.3}Fe(CN)_6$ and $K_{0.6}Ni_{1.2}Fe(CN)_6$ were initially researched as the cathode materials for AAIBs and demonstrated higher intercalation potentials for NH_4^+ ion energy storage compared to Na^+ or K^+ ion energy storage, as evidenced by cyclic voltammetry curves.[22] Since then, additional PBA series such as $(NH_4)_{1.47}Ni[Fe(CN)_6]_{0.88}$ (62.6 mAh g^{-1}),[23] $K_{0.72}Cu[Fe(CN)_6]_{0.78}$ (58.8 mAh g^{-1}),[24] $NaFe^{III}[Fe^{II}(CN)_6]$ (62 mAh g^{-1}),[25] $Na_{1.45}Fe[Fe(CN)_6]_{0.93}$ (73.6 mAh g^{-1}),[26] $Fe_4[Fe(CN)_6]_3$ (61.7 mAh g^{-1}),[27] *etc.* have been formulated and used as cathode materials to achieve electrochemical storage of aqueous NH_4^+ ions. Unfortunately, poor capacities of less than 80 mAh g^{-1} for most reported PBA materials have seriously restricted their practical application in AAIBs.

Metal oxides with a unique layered structure or tunnel structure generally exhibit excellent capacity for aqueous ion energy storage. Consequently, numerous studies have been conducted on the exploratory applications and tentative improvements of metal oxides in aqueous NH_4^+ ion energy storage systems.[28] For example, the capacity of V_2O_5 with a di-layered structure, which provides reasonable density and moderate crystal water through accurate control of the sintering temperature, was as high as 100 mAh g^{-1} with a 0.5 M $(NH_4)_2SO_4$ electrolyte at 0.1 A g^{-1}. Meanwhile, density functional theory (DFT) calculations disclosed the hydrogen bond chemistry of NH_4^+ with V_2O_5, which suggested the climber-swinging model to elaborate the ion migration in V_2O_5.[20] Moreover, the NH_4^+ ion storage capacity of recrystallized MnO_x-40 nanosheets on carbon fibers under the combined effect of Ostwald ripening and Mn^{3+} disproportionation during cycles was 176 mAh g^{-1} with a 0.5 M NH_4Ac electrolyte at 0.5 A g^{-1}.[29] Notably, recent research has confirmed that acetate ions can coordinately interact with manganese on a cathode surface and facilitate NH_4^+ ion adsorption properties, resulting in reduced capacity improvement and resistance to charge transfer.[30] Furthermore, an urchin-like $NH_4V_4O_{10}$ anchored onto a carbon fiber was matched with a polyaniline anode to form NH_4^+ ion full cells, and the capacity was as high as 103 mAh g^{-1} at 0.1 A g^{-1} because of a rapid diffusion path and excellent accommodation capacity for the electrode material to allow reversible shuttling of NH_4^+ ions from the polyaniline anode to the $NH_4V_4O_{10}$ cathode or *vice versa*.[31] Although the above efforts on metal oxides have resulted in considerable breakthroughs in the initial capacity and reaction mechanism for AAIBs, the rate capacity, cycling performance, discharge voltage and compatibility between cathodes and anodes are still unsatisfactory.

Herein, we prepared rutile-phase VO_2 (R–VO_2) microspheres through easy ultrasonic atomization deposition and employed them as cathode materials in AAIBs for the first time. Better capacity, higher working potential, lower electrochemical impedance, and a larger proportion of surface-controlled capacity for NH_4^+ ion energy storage were elucidated through comprehensive electrochemical comparison and analysis with K^+ and Na^+ energy storage. Furthermore, R–VO_2/CNT composite microspheres were synthesized by mixing specific proportions of CNTs into precursors to further advance the rate performance, cycling stability, and discharge capacity. Additionally, energy storage in different voltage ranges was systematically analyzed from both theoretical calculation and experimental comparisons. Finally, the practical application of R–VO_2/CNT composite microspheres was proved by constructing a full cell with a UP anode. Our work provides new potential cathode materials for AAIBs, and offers an efficient candidate approach to promote the electrochemical performance of R–VO_2.

2. Experimental

The ultrasonic atomization deposition method was applied in preparing R–VO_2 microspheres. 3.2 g of V_2O_5 and 4.5 g of $H_2C_2O_4$ were blended within a beaker that contained 60 mL of deionized water. Following 1 h of ultrasonic vibration and 12 h of magnetic stirring at ambient temperature, we obtained the resultant solution and loaded it into ultrasonic atomization equipment for atomization, followed by transport into a tubular furnace under an argon atmosphere. We later deposited solid powders at 600 °C until the solution was exhausted. When the solution was cooled to ambient temperature, we acquired R–VO_2 microspheres. R–VO_2/CNT composite microspheres were achieved, entirely based on the above processes with the additional 1.05 g of CNTs.

3. Results and discussion

Fig. 1a illustrates the ideal crystal model of the R–VO_2, which had a rutile structure and crystallized into the tetragonal $P4_2/mnm$ space group. The V^{4+} atom was connected with 6 equal O atoms to form an edge-sharing $[VO_6]$ octahedron with 2 short (1.91 Å) as well as 4 long (1.99 Å) V–O bonds. The $[VO_6]$ octahedra were repeatedly co-edge stacked along the (001) crystal face and alternately co-vertex accumulated with the vertical state along the (110) crystal face. The V and O atoms were arranged in an orderly fashion to form the skeleton, and thus provided two three-dimensional ion transport tunnels along the (110) and (101) crystal faces, respectively. We also carried out DFT calculations to investigate the lowest energy model configurations of R–VO_2 when charge carriers, such as K^+, Na^+ and NH_4^+ ions, were inserted. Notably, the calculated results confirmed that the carriers were preferentially stored in the (110) crystal face with a more appropriate width of 3.20 Å. When ions were diffused in the relatively narrow (101) crystal face, the crystal lattice was severely distorted and caused the calculation program to crash.

Fig. 1b–d illustrate the clearly different diffusion processes for K^+, Na^+ and NH_4^+ ions. The spherical K^+ and Na^+ ions with non-preferential orientations were entirely dependent on the ionic bond interaction.[20] K^+, Na^+ and NH_4^+ ions could insert into the (110) lattice tunnel during the discharge process, while the lattices underwent drastic distortion due to the huge ion size and rigid repulsion force as the K ions diffused (Fig. 1b). Even though the NH_4^+ ions were of a similar size to the K^+ ions, the tetrahedral NH_4^+ diffusion could depend on coordinated
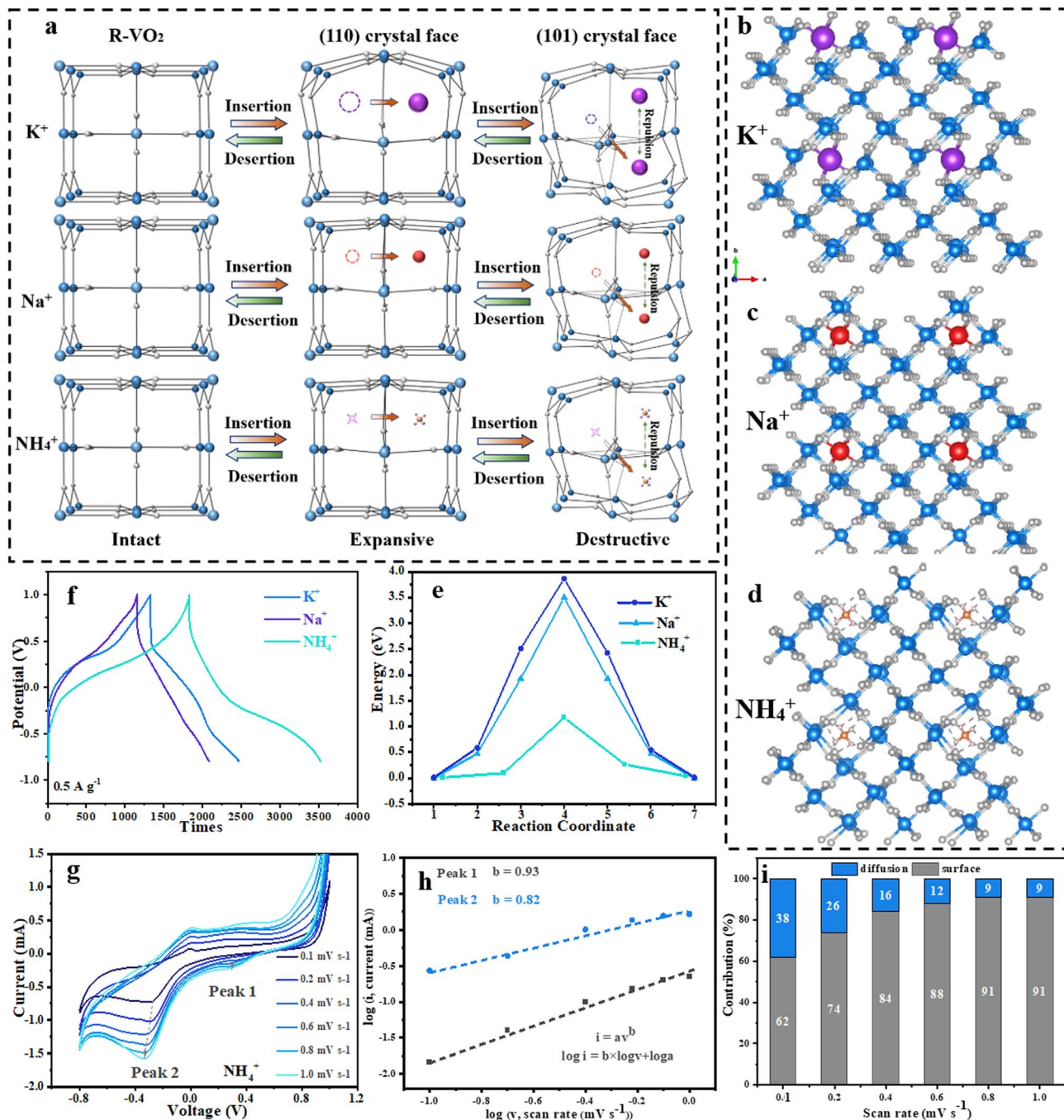
Fig. 1 A diagram of ion diffusion in different tunnels of R–VO$_2$ (a); diffusion barriers for K$^+$ ions, Na$^+$ ions, and NH$_4^+$ ions in R–VO$_2$ (e); chronopotentiometry (CP) profiles (f); the R–VO$_2$ energy storage mechanism for K$^+$ ions (b), Na$^+$ ions (c), and NH$_4^+$ ions (d); cyclic voltammetry (CV) curves at various scan rates of 0.1–1.0 mV s^{-1} for NH$_4^+$ (g); log(i) versus log(v) curves showing cathodic peaks for NH$_4^+$ (h); and diffusion- and surface-controlled contributions to the capacity for NH$_4^+$ (i).

hydrogen bonds with oxygen atoms of R–VO$_2$ along with twisting and rotation for NH$_4^+$ ions (Fig. 1d). A trailing hydrogen bond was broken in the NH$_4^+$ diffusion process, which moved towards the specific oxygen atom undertaking the NH$_4^+$ twist, and this could be imagined as a monkey swinging between trees keeping 3 points still and swinging the body to move forward an arm or leg.[19] The movements were completely different from those of spherical metal ions, and the V–O bonds in the R–VO$_2$

hosts were not affected throughout the entire migration process, which may be the basis for ultrafast electrochemical kinetics and metastable cycling performance.

As shown in Fig. 1e, the NH$_4^+$ diffusion revealed calculated energy barriers of 1.16 eV, which is less than one-third of 3.85 eV for K$^+$ ions, and 3.50 eV for Na$^+$ ions. The interaction of hydrogen bonds rather than ionic bonds and the lighter molar mass resulted in a lower energy barrier for NH$_4^+$ ion diffusion

with respect to K^+ and Na^+ ions. For the saddle point in the NH_4^+ ion diffusion pathway, distances from hydrogen to the adjacent oxygen atom were 1.345 Å, 1.429 Å, 1.627 Å, 1.856 Å and 1.958 Å.

To further compare the electrochemical performances for different charge carriers, systematic electrochemical measurements were conducted in various electrolytes (K_2SO_4, Na_2SO_4 and $(NH_4)_2SO_4$) under the three-electrode test system (Fig. S1). Two evident plateaus could be found for each discharge curve of R–VO$_2$ microspheres for K^+, Na^+ and NH_4^+ energy storage, corresponding to the reversible insertion/extraction of charge carriers in (110) lattice tunnels and (101) lattice tunnels (Fig. 1f). Significantly, the discharge plateaus for NH_4^+ ions were situated at relatively high potentials of 0.3/−0.3 V compared to those for K^+ (0.1/−0.5 V) and Na^+ (0.3/−0.5 V) ions, and were associated with the decreased Gibbs free energy benefiting from the better fit of large NH_4^+ ions into R–VO$_2$ cavities.[22] Additionally, NH_4^+ energy storage achieved a better capacity (222.2 mAh g^{-1}) than K^+ (173.6 mAh g^{-1}) and Na^+ (138.9 mAh g^{-1}). Fig. S2 displays the electrochemical impedance spectroscopy (EIS) for the three charge carriers. Note that NH_4^+ ions delivered a prominent smaller semicircle with a resistance of 5 Ω than K^+ and Na^+ ions, indicating smaller bulk resistance and faster charge-transfer processes for NH_4^+ ions.

The capacity contributions of K^+, Na^+ and NH_4^+ ions in R–VO$_2$ microspheres were determined by cyclic voltammetry (CV) analysis at a scan rate of 0.1–1.0 mV s^{-1} (Fig. 1g–i and S3). There were 2 reduction peak pairs observed in every CV curve for the three ions at various scan rates, which was in exact agreement with the discharge plateaus in Fig. 1f. Significantly, all peaks moved to a lower voltage as the scan rate was increased. Using the peak currents at different scan rates, capacity contributions for K^+, Na^+ and NH_4^+ ions could be qualitatively determined using the equation $i = av^b$.[32] The b values for K^+ ions were calculated to be 0.64 and 0.59 during the discharge process (Fig. S3b), indicating that the capacity was simultaneously contributed to by dominating diffusion control and slight surface control. Na^+ ions exhibited b-values of 0.52 and 0.54, which were closer to the ideal b-value (0.5) (Fig. S3e), implying that diffusion-controlled behavior occurred. In complete contrast to K^+ and Na^+ ions, the high b values of 0.93 and 0.82 for NH_4^+ ions demonstrated a predominantly surface-controlled process (Fig. 1h), which has been proved to be beneficial for faster diffusion kinetics of NH_4^+ ions.[20] The capacity contribution proportions of the three carriers were quantitatively evaluated using the following equation: $i = k_1v + k_2v^{1/2}$. After employing the lowest scan rate (0.1 mV s^{-1}), K^+ ions presented a higher diffusion-controlled contribution of 77% with a small surface-controlled capacity of 23% (Fig. S3c). After increasing the scan rates to 0.1–1.0 mV s^{-1}, the diffusion-controlled contribution decreased to 58%. Na^+ ions exhibited almost diffusion-controlled behavior at each scan rate (Fig. S3f). NH_4^+ ions exhibited a high surface-controlled percentage of 62% at the lowest scan rates (0.1 mV s^{-1}), and this percentage was quickly increased to more than 90% when the scan rates reached 0.8 mV s^{-1} (Fig. 1i). Overall, NH_4^+ ions exhibited higher insertion potential and better reaction kinetics than K^+ and Na^+ ions. This is mainly attributed to the tetrahedral structure of

NH_4^+, which binds stably to the carrier material *via* N–H···O hydrogen bonds, which mitigates structural damage, increases the low desolvation energy and interfacial charge transfer, and results in a lower lattice compatibility and diffusion barrier. Additionally, the high-rate charge storage dominated by pseudocapacitance results in more significant bulk diffusion limitation at high rates, which further amplifies the interfacial advantages of NH_4^+.

On the basis of the superior capacity and fast reaction kinetics for NH_4^+ ions in the R–VO$_2$ microspheres, we developed R–VO$_2$/CNT composite microspheres to further advance the electrochemical performance of R–VO$_2$ microspheres. XRD patterns (Fig. 2a) for R–VO$_2$ as well as R–VO$_2$/CNT composite microspheres were precisely indexed to tetragonal R–VO$_2$ (PDF#74-1642, $P4_2/mnm$ space group), and the lattice parameters were $a = 4.53$ Å, $b = 4.53$ Å, $c = 2.869$ Å, while the R–VO$_2$/CNT composite microspheres additionally exhibited an obvious characteristic peak corresponding to the (200) crystal face of carbon. In particular, it should be mentioned that the crystallinity of the composite microspheres was lower than that of the R–VO$_2$ microspheres from the difference between the XRD patterns. The Raman spectrum exhibited three additional peaks at 1341, 1576 and 2685 cm^{-1} for the R–VO$_2$/CNT composite microspheres, which provided the most reliable evidence for the successful combination of CNTs and R–VO$_2$ (Fig. 2b). The peaks at 1341, 1576, and 2685 cm^{-1} for R–VO$_2$/CNTs are attributed to the characteristic peaks of carbon nanotubes. The peaks detected at 141 and 275 cm^{-1} are due to the bending vibrations of the V–O–V bond backbone. The peaks observed at 520 and 695 cm^{-1} can be attributed to the stretching mode of V–O–V. The peak at 992 cm^{-1} corresponds to the stretching mode of V=O in distorted octahedral and tetrahedral geometries.

XPS measurements were performed to qualitatively evaluate the element chemical composition for R–VO$_2$ as well as R–VO$_2$/CNT composite microspheres. High-resolution V 2p XPS spectra for the two microspheres (Fig. 2e) illustrated 2 separate peaks corresponding to V $2p^{3/2}$ and V $2p^{1/2}$ at 516.5 and 523.7 eV, whose typical spin energy difference of 7.2 eV was in perfect agreement with R–VO$_2$. Moreover, the two microspheres both exhibited a V–O bond peak at 530.2 eV, while the R–VO$_2$/CNT composite microspheres exhibited a C–O bond signal at a higher binding energy of 531.5 eV (Fig. 2d), owing to the C–O functional groups on the surface of the CNTs and the combination of C on the CNT surface and O in R–VO$_2$.

BET measurements presented very different adsorption isotherms for R–VO$_2$ microspheres (Fig. 2f) and R–VO$_2$/CNT composite microspheres (Fig. 2g). The R–VO$_2$ microspheres displayed a concave downward type-III N$_2$ adsorption–desorption isotherm without an inflection point, suggesting a typical physical adsorption process on the surface for non-porous materials. However, the R–VO$_2$/CNT composite microspheres exhibited a type-IV N$_2$ adsorption–desorption isotherm, accompanied by H$_1$-type hysteresis looping, which is usually characterized by uniformly distributed cylindrical holes. Furthermore, the surface area of the R–VO$_2$/CNTs composite microspheres was 7.0588 m^2 g^{-1}, while their pore volume was 0.0416 cm^3 g^{-1}, which were about ten-times higher than those
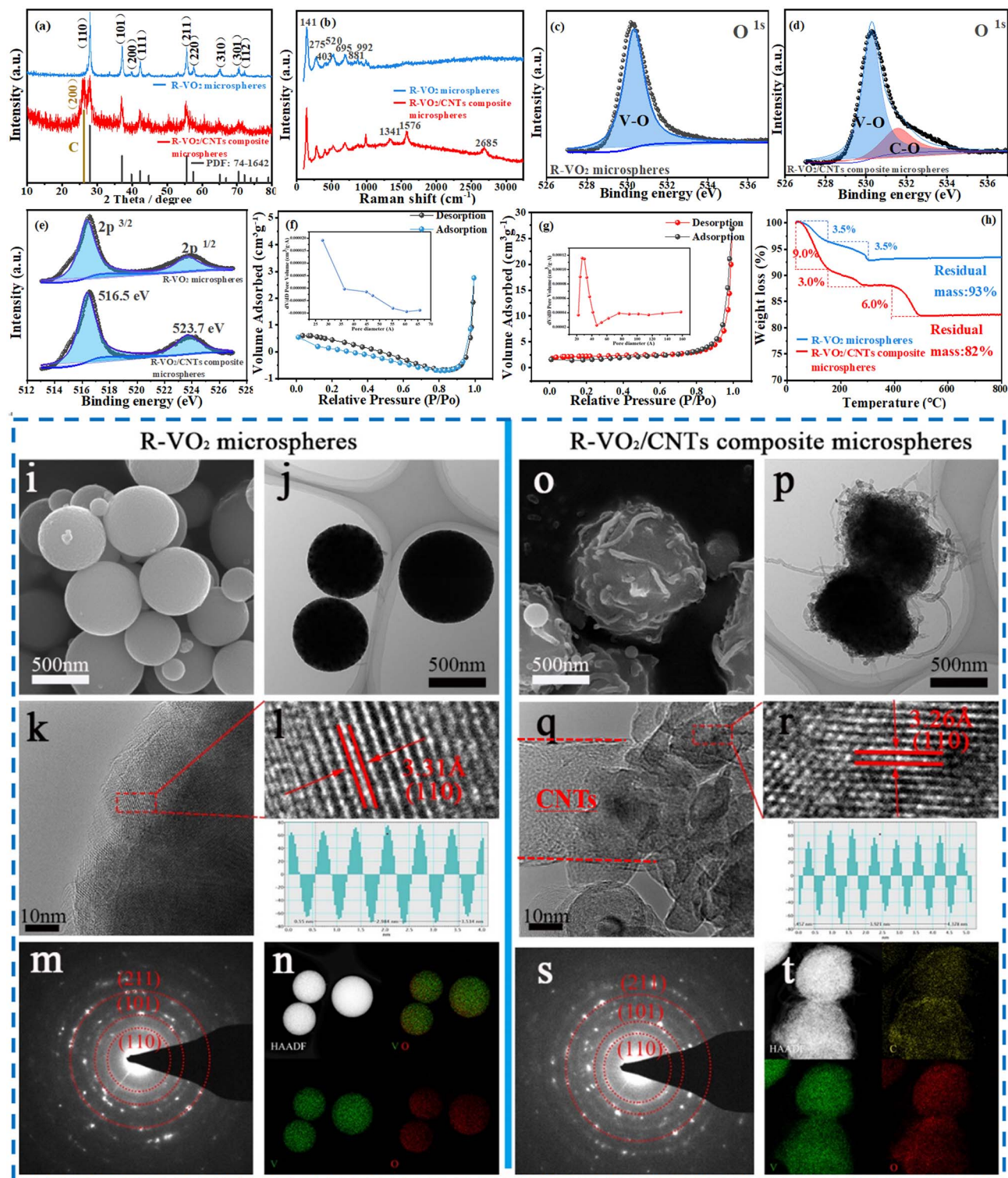
Fig. 2   X-ray diffraction patterns for the 2 microspheres (a), Raman spectra for the 2 microspheres (b), O 1s (c and d) and V2p (e) XPS spectra of the 2 microspheres, adsorption/desorption and pore size distribution curves and relevant pore size distributions of R−VO$_2$ (f) and R−VO$_2$/CNT composite microspheres (g), and TG plots of the two microspheres (h). SEM (i), TEM (j), and HRTEM (k and l) images; SAED patterns (m) and EDS mapping (n) for R−VO$_2$ microspheres. SEM (o), TEM (p), and HRTEM (q and r) images; SAED patterns (s) and EDS mapping (t) for R−VO$_2$/CNT composite microspheres.

for the R–VO$_2$ microspheres whose surface area and pore volume were 0.7834 m^2 g^{-1} and 0.0042 cm^3 g^{-1}, respectively. A larger specific surface area can provide more electrode/electrolyte contact interfaces, expose more V active sites, and enable more thorough adsorption and deintercalation reactions of NH$_4^+$ on the electrode surface, thereby enhancing the actual specific capacity of the battery. In addition, the uniform cylindrical pores corresponding to the H$_1$-type hysteresis loop match the one-dimensional tubular structure of CNTs, forming continuous ion transport paths inside the electrode. On the one hand, the mesoporous structure significantly shortens the solid-phase diffusion distance of NH$_4^+$ and reduces the ion diffusion resistance; on the other hand, the connectivity of the pores avoids the "dead zones" in ion transport caused by the pore-free structure of pure R–VO$_2$, especially during high-rate charging and discharging, effectively alleviating concentration polarization and enhancing the rate performance of the battery. Based on the Barrett–Joyner–Halenda (BJH) model, the pore size distribution was centered at ~30 nm (inset in Fig. 2g), which is in accordance with the diameter of the CNTs. The abundant mesopores in R–VO$_2$/CNT composite microspheres could evidently enhance the contact area of R–VO$_2$ with the electrolyte, while significantly shortening the NH$_4^+$ ion diffusion path. Meanwhile, the large specific surface area could dramatically increase the number of active sites of energy storage in AAIBs.

The CNT contents in the R–VO$_2$/CNT composite microspheres were ascertained from the TGA difference from the R–VO$_2$ microspheres. In the temperature range of 20 to 150 °C, the R–VO$_2$/CNT composite microspheres exhibited more serious weight loss of 9.0% than that of the R–VO$_2$ microspheres of 3.5%. The greater amount of adsorbed water for the R–VO$_2$/CNT composite microspheres was ascribed to the mesoporous composite microspheres providing more abundant storage sites for free water molecules. When the temperature was gradually increased to 300 °C, the two microspheres exhibited similar weight losses of 3.5% and 3%, indicating the release of crystal water. More importantly, the R–VO$_2$/CNT composite microspheres achieved a weight loss of 6% between 400 and 500 °C, demonstrating CNT oxidation.

We conducted SEM and TEM observations to intuitively investigate morphological differences between the R–VO$_2$ microspheres and R–VO$_2$/CNT composite microspheres. The R–VO$_2$ microspheres displayed uniform particles about 500 nm in diameter and extremely smooth surfaces (Fig. 2i and j). The lattice distance of 3.31 Å could be indexed to the (110) plane of R–VO$_2$ (Fig. 2k and l). In particular, it was difficult to distinguish between nano-sheet units and boundaries due to the extremely dense R–VO$_2$ microspheres. The SAED pattern for R–VO$_2$ microspheres (Fig. 2m) exhibited three different diffraction rings for (110), (101) and (211) crystal planes indexed to rutile phase VO$_2$. As demonstrated by EDS mappings (Fig. 2n), V and O showed homogenous distribution within the microspheres. The R–VO$_2$/CNT composite microspheres (Fig. 2o and p) exhibited a larger diameter than the R–VO$_2$ microspheres of about 700 nm, and numerous CNTs were dispersed in the R–VO$_2$/CNT composite microspheres. In particular, it should be mentioned that CNTs with catalytic effects of surface active functional groups accelerated the nucleation processes, resulting in a severe accumulation of structural units in R–VO$_2$/CNT composite microspheres compared to R–VO$_2$ microspheres (Fig. 2q). The lattice spacing of 3.26 Å was assigned to the (110) crystal face of R–VO$_2$ (Fig. 2r) and three diffraction rings in the SAED pattern (Fig. 2s) were perfectly assigned to the (110), (101) and (211) crystal faces for R–VO$_2$. The EDS mappings (Fig. 2t) showed entirely overlapping O and V on the R–VO$_2$/CNT composite microspheres, while the C distribution extended out of the V and O circles. It was suggested that the CNTs perfectly spread through the microspheres, which could be electrolyte reservoirs, reducing ion diffusion distances while promoting charge storage reactions.

CR2016-type AAIBs were assembled to systematically investigate electrochemical performances of R–VO$_2$ microspheres and R–VO$_2$/CNT composite microspheres. Fig. 3a and d show initial 3 CV profiles of R–VO$_2$ as well as R–VO$_2$/CNT composite microspheres at the 0.1 mV s^{-1} scan rate and −1.5–0.8 V voltage range. There were 2 redox peak pairs detected at 0.1/0.3 V and −0.5/−0.1 V, associated with NH$_4^+$ ion diffusion along the (110) crystal face and the (101) crystal face, respectively. The overlapping redox peaks of the first three cycles at higher voltage (0.1/0.3 V) were indicative of highly reversible electrochemical behavior corresponding to (110) crystal face diffusion. Meanwhile, the obviously reduced redox peaks at a lower voltage (−0.5/−0.1 V) signified irreversible electrochemical behavior corresponding to (101) crystal face diffusion, which conformed with DFT analysis. R–VO$_2$ undergoes more irreversible changes under high voltage, with a greater shift in peaks and more capacity degradation, which corresponds to the electrochemical performance of the material. Furthermore, the degree of peak overlap is lower after modification, which is also attributed to the irreversible dissolution of VO$_2$.

Galvanostatic charge and discharge (GCD) measurements of R–VO$_2$ as well as R–VO$_2$/CNT composite microspheres were performed in the −1.3–0.8 V range at the 0.05 A g^{-1} current density (Fig. 3b and e). There were 2 voltage plateau pairs detected at 0.1/0.3 V and −0.5/−0.1 V on each GCD curve, which were associated with redox peaks in the CV curves. The oxidation peak at 0.3 V and reduction peak at 0.1 V correspond to reversible electrochemical reaction processes of NH$_4^+$ along the (110) crystal plane of VO$_2$, while the oxidation peak at −0.1 V and reduction peak at −0.3 V correspond to irreversible electrochemical reactions of NH$_4^+$ along the (101) crystal plane of VO$_2$.

Impressively, R–VO$_2$/CNT composite microspheres reached an excellent capacity (950 mAh g^{-1}) in cycle 1, far exceeding R–VO$_2$ microspheres (560 mAh g^{-1}). The capacity of R–VO$_2$/CNT composite microspheres remained high (715 mAh g^{-1}) after three cycles, while R–VO$_2$ microspheres retained only 520 mAh g^{-1}. The introduction of carbon nanotubes, on the one hand, allows the composite microspheres to exhibit a rich mesoporous structure and a larger specific surface area, thereby exposing more energy storage sites and significantly enhancing capacity. On the other hand, due to the perfect penetration of carbon nanotubes, the shortened ion diffusion path and improved conductivity can significantly promote reaction
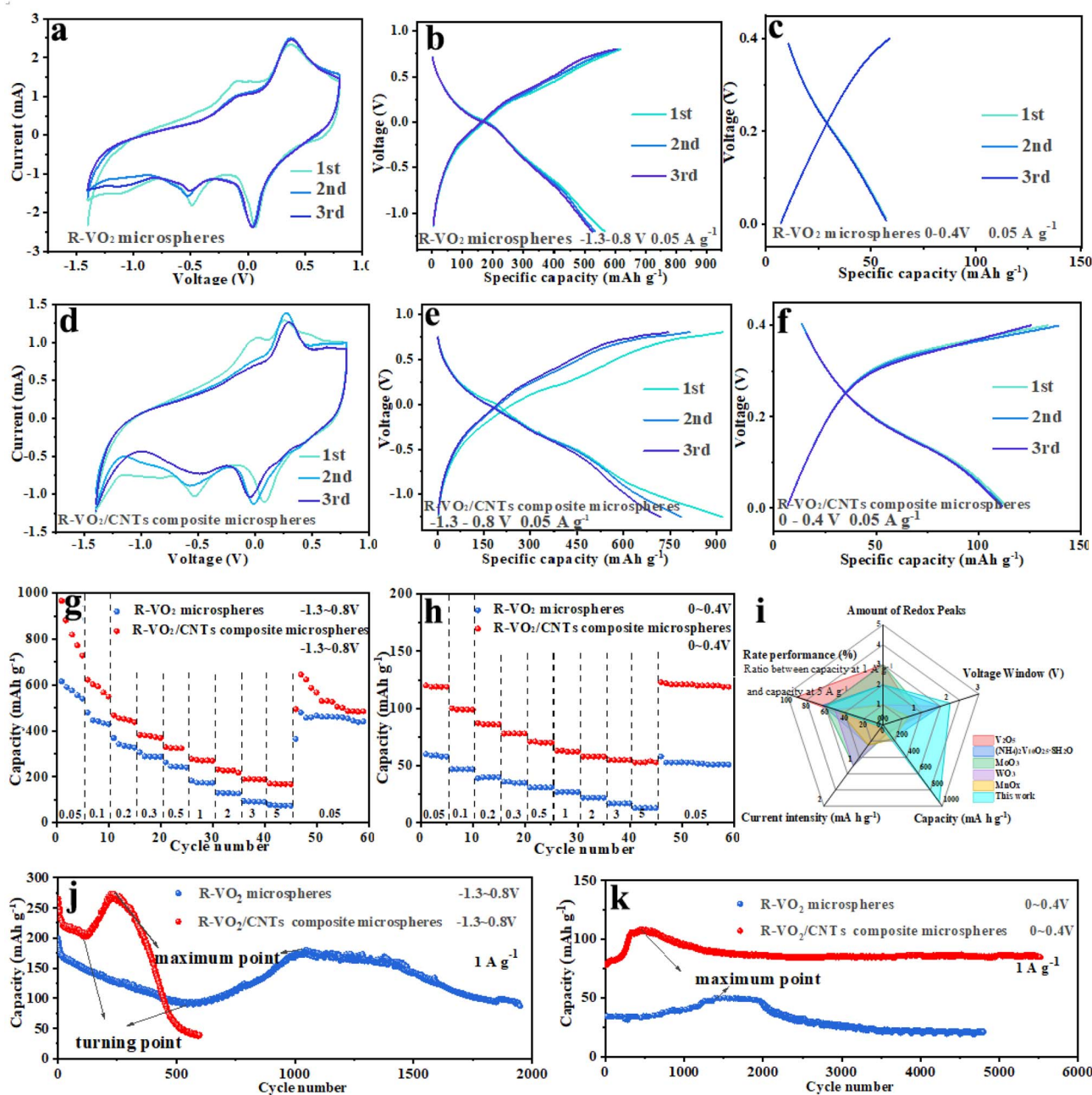
Fig. 3 CV curves for R−VO$_2$ (a) as well as R−VO$_2$/CNT composite microspheres (d) at 0.1 mV s^{-1}, GCD curves for R−VO$_2$ (b) as well as R−VO$_2$/CNT composite microspheres (e) during the first 3 cycles at 0.05 A g^{-1} between −1.3 V and 0.8 V, GCD curves for R−VO$_2$ (c) and R−VO$_2$/CNT composite microspheres (f) during the first 3 cycles at 0.05 A g^{-1} between 0 V and 0.4 V, and rate performance together with long-term cycling performance for both microspheres at −1.3−0.8 V (g and j) and at 0−0.4 V (h and k). Comparison of the electrochemical performance of numerous metallic oxides (i).

kinetics, resulting in considerable rate performance. However, ultrafast reaction kinetics exacerbate the lattice structure damage of the tunnel at lower voltages (101), leading to the dissolution of VO$_2$ and subsequent capacity decay. The observations in Fig. 3b and d reveal that the discharge capacity fade for the two microspheres in the initial three cycles mainly occurred at voltage ranges below 0 V, while when the voltage exceeded 0 V there was very little variation. Therefore, we employed a voltage of 0–0.4 V to further determine the

correspondence between voltage and capacity. As depicted in Fig. 3c and f, no capacity fading could be detected for R−VO$_2$ or R−VO$_2$/CNT composite microspheres during the first three cycles. This perfectly validated the DFT results indicating that (110) crystal faces were more suitable for the reversible NH$_4^+$ insertion and extraction than (101) crystal faces. Additionally, the R−VO$_2$/CNT composite microspheres delivered a surprisingly exceptional initial capacity (120 mAh g^{-1}), twice that of R−VO$_2$ microspheres at 60 mAh g^{-1}.

Rate capabilities for the two microspheres at a voltage of −1.3–0.8 V are evaluated in Fig. 3g. R–VO$_2$/CNT composite microspheres revealed a markedly increased capacity relative to R–VO$_2$ microspheres under different current densities. As the current density increased between 0.05 and 5 A g^{-1}, the 2 microspheres both displayed slightly reduced capacity. At the greatest current density at 5 A g^{-1}, the R–VO$_2$/CNT composite microspheres maintained a significant capacity (170 mAh g^{-1}), more than two times that of the R–VO$_2$ microspheres of 75 mAh g^{-1}. Furthermore, we compared the rate capabilities at 0–0.4 V for different microspheres (Fig. 3h). When the current densities increased between 0.05 and 5 A g^{-1}, the R–VO$_2$/CNT composite microsphere series had capacities of 120, 99, 86, 78, 70, 62, 58, 55, and 53 mAh g^{-1}, surpassing the values for the R–VO$_2$ microsphere series of 59, 47, 39, 35, 31, 27, 22, 17, and 13 mAh g^{-1} under the equivalent current densities. With the reduction of the current density to 50 mA g^{-1}, the R–VO$_2$/CNT composite microspheres recovered increased capacity (123 mAh g^{-1}), whereas the capacity of the R–VO$_2$ microspheres remained at 58 mAh g^{-1}. In general, at any voltage range and current density, R–VO$_2$/CNT composite microspheres exhibited a higher absolute capacity than R–VO$_2$ microspheres, which signified that fabrication of the composite microsphere structure with CNTs was an effective strategy to increase the R–VO$_2$ capacity. Compared with various reported oxides, R–VO$_2$/CNT composite microspheres displayed unparalleled capacity and excellent rate performance (Fig. 3i).

Unfortunately, poor capacity retention was delivered by R–VO$_2$/CNT composite microspheres during long-cycling performance testing at −1.3–0.8 V at 1 A g^{-1} (Fig. 3j). The two microspheres both displayed significant fluctuation of the cycling capacity, attributed to the combination of the two opposite forces of material activation and material dissolution. An abrupt capacity fade for the two microspheres was evidenced in the first cycles, resulting from a few microspheres with poor crystallinity being rapidly destroyed and dissolved with continuous volume changes. Thereafter, the capacity fading became gradually slower, and even stopped at a turning point. This was owing to the material activation which could offer obvious capacity increase and offset the capacity decrease due to the lattice structure destruction. With the increasing material activation, the capacity was increased significantly and reached a maximum value after numerous cycles. The emergence of the maximum point meant that the material activation for R–VO$_2$ was generally completed, and then the capacity dropped drastically due to the material breakdown and dissolution. Significantly, the R–VO$_2$/CNT composite microspheres acquired increased initial capacity (275 mAh g^{-1}) compared with the R–VO$_2$ microspheres (200 mAh g^{-1}). In particular, the R–VO$_2$/CNT composite microspheres exhibited better capacities (200 and 280 mAh g^{-1}) at the turning point and maximum point, almost twice those of the R–VO$_2$ microspheres (100 and 175 mAh g^{-1}). Additionally, the turning point and maximum point for the R–VO$_2$/CNT composite microspheres were located at 100 cycles and 200 cycles, much earlier than those for the R–VO$_2$ microspheres at 500 cycles and 1000 cycles. Nevertheless, the R–VO$_2$/CNT composite microspheres deliver much worse capacity

retention than the R–VO$_2$ microspheres, and the capacity decays by more than 90% after only 600 cycles. The above results indicate that fabricating composite microspheres obviously affected R–VO$_2$'s electrochemical properties. First, the abundant mesopores and large specific surface area of the composite microspheres could expose more energy storage sites to greatly enhance the capacity; second, the ion diffusion pathway reduction and electrical conductivity improvement benefiting from perfect CNT penetration could be observed to promote the reaction kinetics, leading to the considerable rate performance. However, the ultra-fast reaction kinetics exacerbated the lattice structure destruction for the (101) tunnels at lower voltage.

Durability and long-term cycling stability for the two microspheres were studied at 0–0.4 V (Fig. 3k). During the initial cycles, the capacity for the R–VO$_2$/CNT composite microspheres gradually increased between 75 mAh g^{-1} and 115 mAh g^{-1} and was maintained for 200 cycles. During the 5000th cycle, the R–VO$_2$/CNT composite microspheres could still retain considerable capacity (85 mAh g^{-1}), 113% of the initial capacity and 78% of the maximum capacity. Meanwhile, the capacity of the R–VO$_2$ microspheres increased from 31 mAh g^{-1} to 50 mAh g^{-1} in the first 1300 cycles, and was only 20 mAh g^{-1} in the 5500th cycle (65% of the initial capacity and 40% of the maximum capacity).

The cycling tolerances of R–VO$_2$ microspheres and R–VO$_2$/CNT composite microspheres under different voltage ranges were elaborated by SEM and TEM observations (Fig. 4). When R–VO$_2$ microsphere and R–VO$_2$/CNT composite microsphere electrodes were employed at −1.3–0.8 V, the two electrodes both exhibited obvious and severe damage during the repetitive charge and discharge processes, but exhibited very different cycling durability. Compared with the smooth surface for the initial R–VO$_2$ microspheres (Fig. 4a and f), R–VO$_2$ microspheres displayed a rougher surface (Fig. 4b), and loose and slightly damaged microspheres (Fig. 4g) after 1000 cycles. After 3000 cycles (Fig. 4c and h), the R–VO$_2$ microspheres have been completely destroyed except for some tablets formed by binders. Nevertheless, R–VO$_2$/CNT composite microspheres encountered more serious and faster destruction. The R–VO$_2$/CNT composite microspheres exhibited critical fractures (Fig. 4l and q) after only the 200th cycle (turning point), even up to the 1000th cycle, and nothing else was discovered except for intertwined CNTs (Fig. 4m and r). This was closely related to the ultra-high surface activity and extremely low crystallinity of the carbon nanotube composite microspheres.

At 0–0.4 V, the cycling stability for R–VO$_2$ and R–VO$_2$/CNT composite microspheres was significantly improved. For cycled R–VO$_2$ microspheres, the pristine structure was perfectly maintained and the surface of the microspheres was smooth without any pulverization after 1000 cycles (Fig. 4d). Even upon cycling to 3000 cycles, only slight cracks occurred on the microsphere surface (Fig. 4e), while the interior of the R–VO$_2$ microspheres maintained a prominent close-packing architecture (Fig. 4i). Meanwhile, the R–VO$_2$/CNT composite microspheres retained high integrity after 3000 cycles. The excellent stability of the R–VO$_2$ microspheres (Fig. 4j) and R–VO$_2$/CNT composite microspheres (Fig. 4t) was clearly confirmed by the TEM images, in which the structures remained consistent with
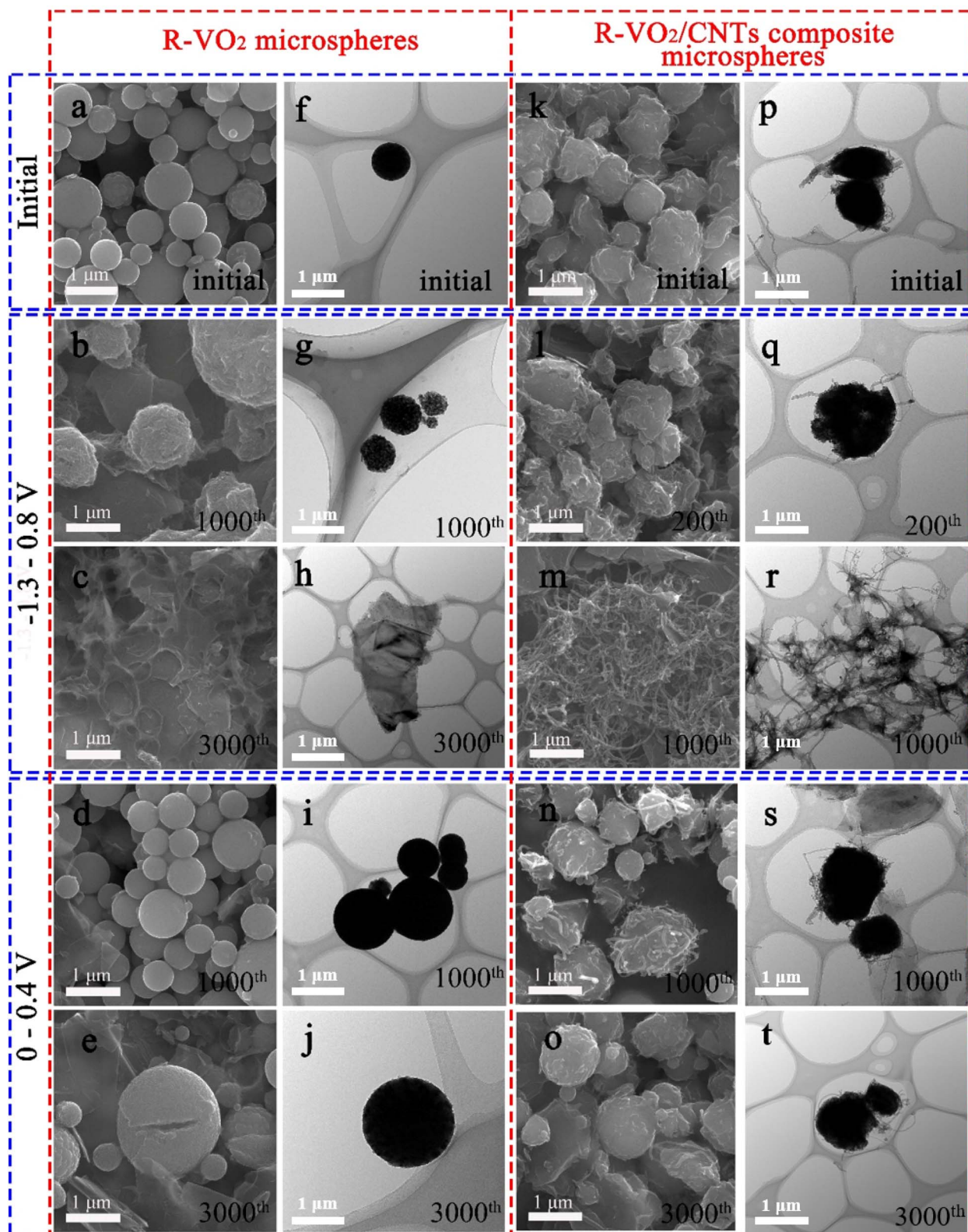
Fig. 4 SEM images showing electrodes of R−VO$_2$ microspheres in selected states: initial (a), after 1000 (maximum point) (b) and 3000 (c) cycles at −1.3−0.8 V, and after 1000 (d) and 3000 (e) cycles at 0−0.4 V. TEM images showing electrodes of R−VO$_2$ microspheres in selected states: initial (f), after 1000 (g) and 3000 (h) cycles at −1.3−0.8 V, and after 1000 (i) and 3000 (j) cycles at 0−0.4 V. SEM images showing electrodes of R−VO$_2$/CNT composite microspheres in selected states: initial (k), after 200 (maximum point) (l) and 1000 (m) cycles at −1.3−0.8 V, and after 1000 (n) and 3000 (o) cycles at 0−0.4 V. TEM images showing electrodes of R−VO$_2$/CNT composite microspheres in selected states: initial (p), after 200 (q) and 1000 (r) cycles at −1.3−0.8 V, and after 1000 (s) and 3000 (t) cycles at 0−0.4 V.

the initial structure after long-term cycling. The electrodes exhibited distinct structure stability within different voltage ranges, which was related to the sequential NH_4^+ insertion into the (110) and (101) crystal faces. Adjusting the charging and discharging voltage range, abandoning unrealistic capacities below 0 V, and avoiding structural collapse caused by ion insertion into the (101) crystal plane can effectively promote the practical application process of the batteries.

The reaction kinetics for the two microspheres were evaluated through electrochemical impedance spectroscopy (EIS) (Fig. 5a, Table S1). The ohmic resistance (R1) and charge transfer resistance (R2) for the R–VO$_2$/CNT composite microspheres were smaller than those of the R–VO$_2$ microspheres. This was attributed to the construction of the CNT conductive networks in the R–VO$_2$ microspheres. Moreover, the R–VO$_2$/CNT composite microspheres exhibited lower Warburg impedance (Z_w), suggesting that the CNT introduction efficiently decreased the NH_4^+ diffusion resistance and shortened the NH_4^+ diffusion distance. The diffusion coefficients for the R–VO$_2$ microspheres and R–VO$_2$/CNT composite microspheres were confirmed using GITT technology (Fig. 5b and c). The diffusion coefficients for the two microspheres gradually decreased in the discharge process and increasingly grew in the charge process. Additionally, the NH_4^+ diffusion coefficients for R–VO$_2$/CNT composite microspheres were between $10^{-5.0}$ and $10^{-5.8}$ cm^2 s^{-1} during discharge, and were markedly increased relative to R–VO$_2$ microspheres (between $10^{-5.5}$ and $10^{-6.8}$ cm^2 s^{-1}). In the charge process, the R–VO$_2$/CNT composite microspheres exhibited increased NH_4^+ diffusion coefficients (between $10^{-6.3}$ and $10^{-4.9}$ cm^2 s^{-1}) compared with the R–VO$_2$ microspheres (between $10^{-6.5}$ and $10^{-5.1}$ cm^2 s^{-1}). These results demonstrated that the NH_4^+ transportation was successfully improved by fabricating the composite microspheres.

The capacity contributions of the R–VO$_2$ microspheres (Fig. S4a) and R–VO$_2$/CNT composite microspheres (Fig. 5d) were also analyzed through CV analysis as scan rates increased between 0.1 and 1.0 mV s^{-1}. This was based on the empirical equation $i = av^b$.[32] b-values for R–VO$_2$ as well as R–VO$_2$/CNT composite microspheres were 0.73/0.84 (Fig. S4b) and 0.80/0.85 (Fig. 5e), respectively. Then, the capacitive contribution was quantitatively evaluated using the equation $i = k_1v + k_2v^{1/2}$. As the scan rate increased between 0.1 and 1.0 mV s^{-1}, the proportion of the surface-controlled process of the R–VO$_2$ microspheres gradually increased from 64% to 91% (Fig. S4c), whereas the R–VO$_2$/CNT composite microspheres also revealed an increasing proportion from 71% to 94% (Fig. 5f). Note that the R–VO$_2$/CNT composite microspheres presented an evidently more surface-controlled process than the R–VO$_2$ microspheres at any scan rate, which was caused by the CNT introduction contributing more surface pseudo-capacitance for the R–VO$_2$/CNT composite microspheres.

The structure conversions in the R–VO$_2$ and R–VO$_2$/CNT composite microspheres were investigated through *in situ* XRD technology during the NH_4^+ insertion/extraction processes. The two microspheres exhibited similar conversion regulation in the charge/discharge processes. As shown in Fig. 5h and S5a, no new diffraction peak was found in the XRD patterns for the R–

VO$_2$ microspheres and R–VO$_2$/CNT composite microspheres. However, some minor changes could be observed in the local amplified XRD patterns for the (110) and (101) diffraction peaks (Fig. 5i and S5b). With the increase of the discharge process, the (110) peaks gradually moved to lower angles until discharge at −0.5 V, but no deviation was noticed until the discharge end (−1.3 V), indicating lattice expansion due to the insertion of NH_4^+ ions into R–VO$_2$. During the charge process, the (110) diffraction peaks exhibited no variations from −1.3 V to −0.5 V, and subsequent recovery of the initial states was observed, suggesting lattice shrinkage caused by the extraction of NH_4^+ ions from R–VO$_2$. The (101) diffraction peaks exhibited distinct changes compared to the (110) diffraction peaks (Fig. 5j and S5c). The (101) diffraction peaks exhibited some major changes only below −0.5 V. The (101) diffraction peaks exhibited obvious deviations towards lower angles from −0.5 V to −1.3 V but could be rapidly recovered upon charging to −0.5 V, suggesting NH_4^+ ion insertion/extraction alone on the (101) crystal lattice. These conclusions perfectly evidence the above-mentioned DFT results.

NH_4^+ ion insertion/extraction in R–VO$_2$ microspheres (Fig. S6) and R–VO$_2$/CNT composite microspheres (Fig. 5k–m) were demonstrated by *ex situ* XPS techniques. The evident N[1s] signal peaks from the survey XPS spectra appeared and disappeared at 400 eV in the discharge and charge processes, indicating highly reversible NH_4^+ insertion/extraction in the R–VO$_2$ microspheres and R–VO$_2$/CNT composite microspheres, which was in exact agreement with the *in situ* XRD results. The transformation of V oxidation valence states which were obtained from the high-resolution XPS spectra further demonstrated the NH_4^+ insertion/extraction processes in the R–VO$_2$/CNT composite microspheres (Fig. 5l and m). Just the V^{4+} signal (V 2p$^{3/2}$, 516.4 eV; V 2p$^{1/2}$, 524.0 eV) could be observed on the pristine cathodes for the R–VO$_2$/CNT composite microspheres. In the fully discharged state, substantial V (54%) was reduced to the +3 valence state (V 2p$^{3/2}$, 515.0 eV; V 2p$^{1/2}$, 522.5 eV), which was attributed to the NH_4^+ insertion. A partial amount of +4 V (46%) was not transferred into lower states, which could be shown in previously reported aqueous batteries.[33,34] In the fully charged state, the reduced V (+3) was converted to a higher valence state (+4) due to the NH_4^+ extraction from R–VO$_2$ crystal lattices. In particular, it should be mentioned that a minor amount of +3 V (13%) was not completely oxidized. It was concluded that the strongly irreversible electrochemical insertion/extraction processes below −0.5 V brought about the difficult conversion for the partial amount of low valence state V. The residual V^{3+} is not directly related to the complete removal of NH_4^+, but rather represents an independent and irreversible process within the system. It originates from abnormal charge compensation pathways and local structural defects, which prevent some V^{3+} from being oxidized to V^{4+}. During charging, the increase in the positive electrode potential preferentially initiates oxygen evolution or NH_4^+ oxidation side reactions, consuming electrons and preventing the oxidation of some V^{3+}. The evolution of O$_2$, a product of these side reactions, does not affect the removal of NH_4^+, resulting in the absence of N in the XPS spectra but the residual presence of V^{3+}. On the
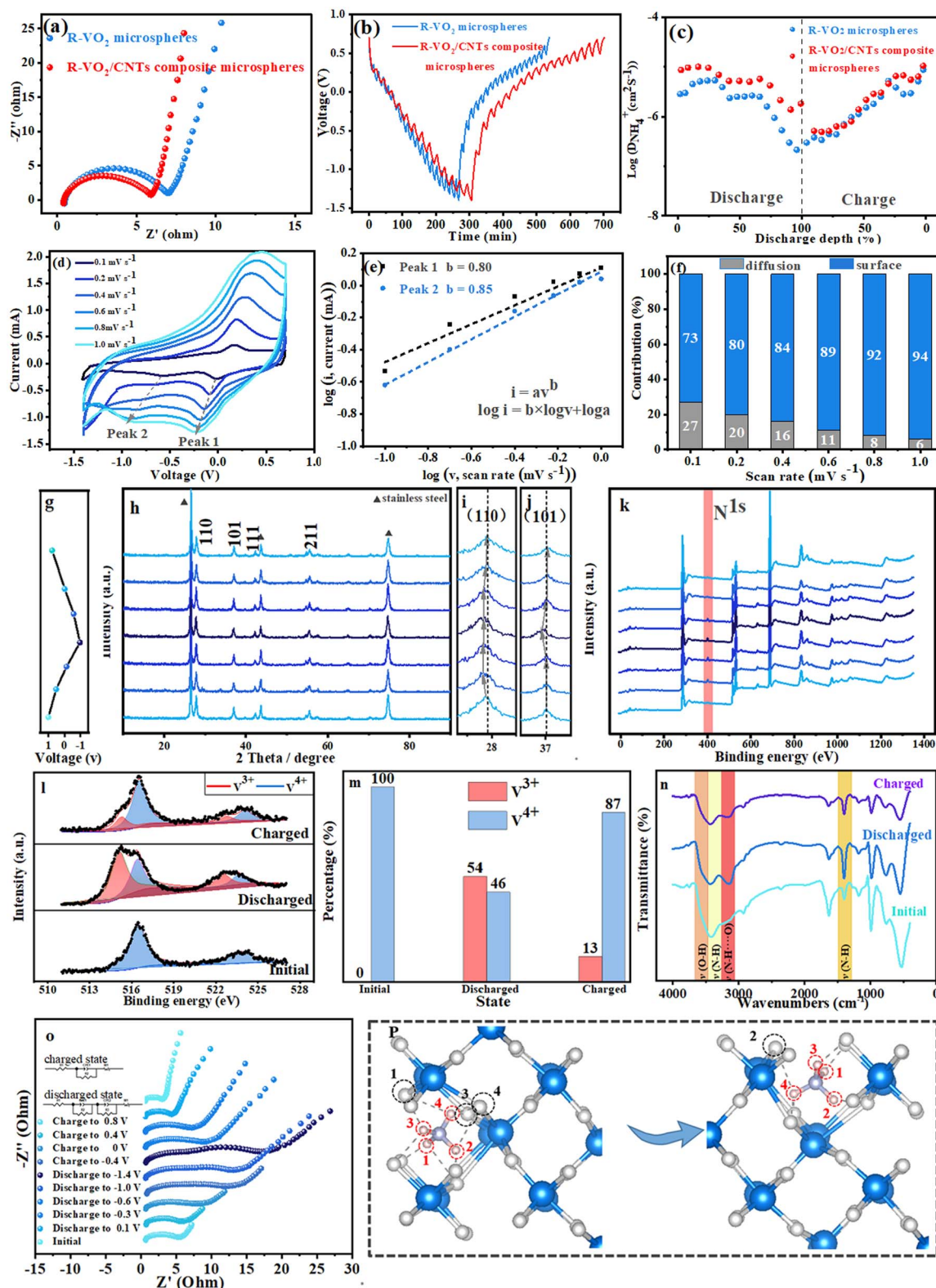
Fig. 5 Electrochemical impedance spectra (a), galvanostatic intermittent titration technique (GITT) curves at 0.05 A g^{-1} (b), NH$_4^+$ diffusion coefficients at different discharge depths (c), CV curves of R−VO$_2$/CNT composite microspheres at 0.1–1.0 mV s^{-1} (d), log(i) $versus$ log(v) curves showing cathodic peaks of R−VO$_2$/CNT composite microspheres (e), surface-controlled and diffusion-controlled contributions to the capacity of R−VO$_2$/CNT composite microspheres (f), ex $situ$ XRD patterns (g–j), ex $situ$ XPS spectra (k–m) and ex $situ$ FTIR spectra (n) of R−VO$_2$/CNT composite microspheres in cycle 1 in different discharge/charge states, in $situ$ electrochemical impedance of R−VO$_2$/CNT composite microspheres in cycle 1 (o), and bond evolution stages during the NH$_4^+$ diffusion process in R−VO$_2$ (p).

other hand, the evolution of O_2 creates oxygen vacancies in VO_2, forming local electron traps. The trapped electrons stabilize V^{3+}, preventing its oxidation during charging. These defects do not alter the hydrogen bonding and removal pathways of NH_4^+, which remain independent.

Hydrogen bond building and breaking in NH_4^+ with R–VO_2 were shown by FT-IR analysis (Fig. 5n). The IR region of 3100–3600 cm^{-1} was associated with overlapping OH and NH bands,[35] that of 3300–3400 cm^{-1} was associated with unperturbed N–H groups, and that of 3100–3300 cm^{-1} was associated with bonded N–H. After the full discharge, an obvious signal at 3170 cm^{-1} stood out relative to the pristine electrode of the R–VO_2/CNT composite microspheres, suggesting that hydrogen bonds (N–H···O) were formed between NH_4^+ and the R–VO_2 host. Upon fully charging, the broad peak at 3170 cm^{-1} was difficult to observe, suggesting that the NH_4^+ insertion/ extraction in the R–VO_2 host were entirely reversible processes. These results indicated that the NH_4^+ insertion/ extraction were related to hydrogen bonding/debonding in the R–VO_2 host. For the reduced R–VO_2 cathode, a small part of the charge was shifted from V (yellow lobes on vanadium) to the H...O=V bond (blue cloud) via the O=V bond, thereby leading to oxidization of the attached V ion (yellow core under the outer blue lobes of the V ion) (Fig. S6).[36]

Charge transfer and ion diffusion for the R–VO_2/CNT composite microspheres during the charge/discharge processes were resolved through in situ EIS methods (Fig. 5o, Table S2 and SI). In the initial state, the Nyquist plots for the R–VO_2/CNT composite microspheres included one high-frequency semicircle and one low-frequency straight line. Upon discharging, the Nyquist plot became a semicircle of gradually increasing size and a straight line with a smaller slope, demonstrating the more difficult ion diffusion and charge transfer due to greater electrochemical polarization. Upon discharge to −0.5 V, a new semicircle emerged within the middle-frequency region, which gradually expanded during subsequent discharge processes, suggesting that the generation of the new semicircle was closely related to the NH_4^+ insertion into the (101) crystal plane. Upon charging, the semicircle within the middle-frequency region preferentially disappeared. Subsequently, the semicircle within the high-frequency region became smaller, while the slope of the straight line within the low-frequency region successively increased, indicating highly reversible extraction of the R–VO_2 host.

Fig. 5p illustrates the evolution of bonding when NH_4^+ ions migrated in R–VO_2 driven by the electric field force, the H···O bonds for H_1, H_2 and H_3 with the adjacent O atoms were successively disconnected, and meanwhile they rotated forward with a central axis of H_4 to form new H···O bonds. H_4 invariably maintained a coupling relationship with O_3 and O_4, but the new H···O bond with O_1 replaced the H···O bond to O_2.

Full cells with a typical "rocking chair" working principle were assembled using a R–VO_2/CNT composite microsphere cathode coupled with a UP anode to exploit the practical applications (Fig. 6a). Fig. 6b shows the initial 3 consecutive CV curves for full cells at −0.25 to 1.1 V. Numerous redox peaks were observed in charge and discharge processes, in which 2 peak pairs detected at −0.1/0.45 V and 0.5/0.75 V were associated with NH_4^+ ion insertion into the R–VO_2/CNT composite microsphere cathode, while others were attributed to UP anode energy storage. Predictably, all reduced peaks displayed extreme instability in voltage position and peak intensity upon cycling.
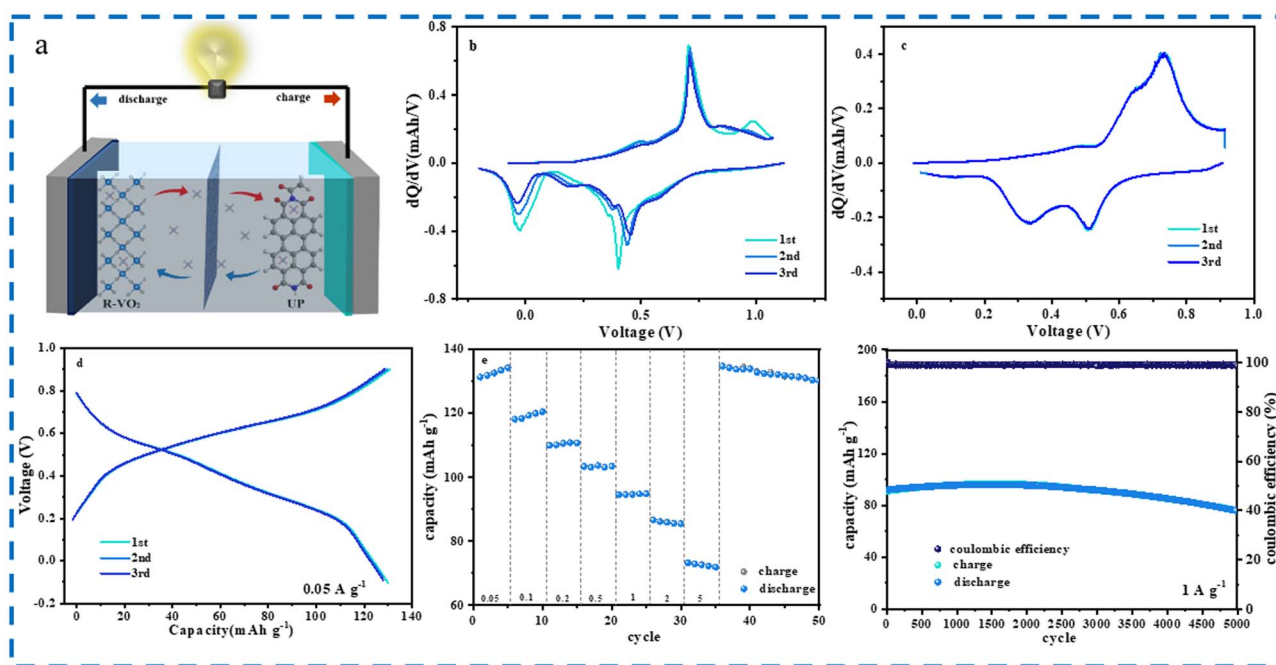

Fig. 6 A schematic diagram showing the aqueous NH_4^+ ion full cell (a), CV curves showing the aqueous NH_4^+ ion full cell from −0.25 V to 1.1 V (b), CV curves showing the aqueous NH_4^+ ion full cell from 0 V to 0.9 V (c), GCD curves for the full cell in the first 3 cycles (d), rate (e) and cycle (f) performances of the full cell.

Thus, the selected voltage range of 0–0.9 V was further employed in CV tests (Fig. 6c). There were 2 obvious redox peak pairs situated at 0.3/0.6 V and 0.5/0.75 V, associated with NH_4^+ ion energy storage for the UP anode and R–VO_2/CNT composite microsphere cathode, respectively. More importantly, the nearly overlapping CV curves for the initial 3 cycles indicated the highly reversible NH_4^+ ion energy storage at this voltage range.

GCD analyses of full cells were conducted at the 0–0.9 V voltage and 0.05 A g^{-1} current density (Fig. 6d). The capacity of the full cell was 130 mAh g^{-1} without any visible capacity decay during the first three cycles. As the current density increased within 0.05–5 A g^{-1} (Fig. 6e), the capacity for the full cell gradually decreased. In particular, the 70 mAh g^{-1} capacity was retained at a high current density of 5 A g^{-1}. After reducing the current density to 0.05 A g^{-1}, the full cell could perfectly recover the initial capacity of 130 mAh g^{-1}. Fig. 6f shows the cycling capacity, and associated coulombic efficiency *versus* cycle number at 1 A g^{-1}. After 2500 cycles, the full cell exhibited a significant capacity of 90 mAh g^{-1} with a high coulombic efficiency reaching almost 100%. Subsequently, this battery exhibited slight capacity decay to 80 mAh g^{-1} after 5000 cycles. These results confirmed excellent rate and cycle performances, which indicated that NH_4^+ ion full cells have potential and are practical for future industrialization.

4. Conclusions

In summary, DFT theoretical calculations revealed that R–VO_2 could provide two ion storage tunnels along the (110) and (101) crystal planes to allow ammonium ions to undergo ultrafast diffusion through unique hydrogen bonds. Furthermore, we successfully prepared R–VO_2/CNT composite microspheres through ultrasonic atomization deposition, and they exhibited increased numbers of active sites and shortened ion diffusion pathways compared to R–VO_2 microspheres. Consequently, R–VO_2/CNT composite microspheres delivered a significant initial capacity (950 mAh g^{-1}) at 0.05 A g^{-1} and an outstanding rate capacity (170 mAh g^{-1}) at 5 A g^{-1} at −1.3–0.8 V. Moreover, a more reasonable voltage range located at 0–0.4 V could be used by combining DFT theoretical calculations and intuitive electron microscopy observations, which could further maintain the cycling stability of R–VO_2/CNT composite microspheres, fully reflecting the practical value of AAIBs. Finally, a groundbreaking full cell with a R–VO_2/CNT composite microsphere cathode and UP anode was proposed and exhibited considerable capacity (130 mAh g^{-1}) at 0.05 A g^{-1} as well as impeccable capacity retention (100%) following 2500 cycles within the 0–0.9 V voltage range. Our investigations offer a reliable strategy for improving R–VO_2 electrode materials and will hopefully stimulate future designs of an advanced novel generation of AAIBs.

Author contributions

Lin-bo Tang and Xian-kai Fan were responsible for the original draft. Wei Zhou and Wei-na Deng were responsible for data curation. Hai Zhu was responsible for validation. Liang Chen was responsible for formal analysis. Jun-chao Zheng and Han Chen were responsible for review and editing.

Conflicts of interest

The authors declare that they have no conflicts of interest.

Data availability

Data are available on request from the authors. The data that support the findings of this study are available from the corresponding author [Junchao Zheng, jczheng@csu.edu.cn] upon reasonable request.

Supplementary information (SI): experimental instruments, testing methods, charts, tables, and further analyses to ensure the reproducibility of the data and the accuracy of interpretation. See DOI: https://doi.org/10.1039/d5sc08747c.

Acknowledgements

References

1 B. Dunn, H. Kamath and J. M. Tarascon, Electrical energy storage for the grid: a battery of choices, *Science*, 2011, **334**(6058), 928–935.

2 S. Chu and A. Majumdar, Opportunities and challenges for a sustainable energy future, *Nature*, 2012, **488**(7411), 294–303.

3 J. Tang, J. Li, P. Pishva, R. Xie and Z. Peng, Aqueous, Rechargeable Liquid Organic Hydrogen Carrier Battery for High-Capacity, Safe Energy Storage, *ACS Energy Lett.*, 2023, **8**(9), 3727–3732.

4 Q. Lu, Y. Jie, X. Meng, A. Omar, D. Mikhailova, R. Cao, S. Jiao, Y. Lu and Y. Xu, Carbon materials for stable Li metal anodes: challenges, solutions, and outlook, *Carbon Energy*, 2021, **3**(6), 957–975.

5 F. Degen, M. Winter, D. Bendig and J. Tubke, Energy consumption of current and future production of lithium-ion and post lithium-ion battery cells, *Nat. Energy*, 2023, **8**(11), 1284–1295.

6 H. Long, Z. H. Wen, M. Wang and Y. Qian, Self-assembled biomolecular 1D nanostructures for aqueous sodium-ion battery, *Advanced Science*, 2018, **5**(3), 1700634.

7 B. Tang, L. Shan, S. Liang and J. Zhou, Issues and opportunities facing aqueous zinc-ion batteries, *Energy Environ. Sci.*, 2019, **12**(11), 3288–3304.

8 S. Wu, X. Zhu, L. Sun, S. Zhang, Z. Wang, X. Zhang, F. Yang, H. Zhang and W. Hu, Materials chemistry for rechargeable zinc-ion batteries, *Chem. Soc. Rev.*, 2020, **49**(13), 4203–4219.

9 B. Tang, L. Shan, S. Liang and J. Zhou, Issues and opportunities facing aqueous zinc-ion batteries, *Energy Environ. Sci.*, 2019, **12**(11), 3288–3304.

10 M. Kumar and T. C. Nagaiah, Efficient production of hydrogen from H_2S via electrolysis using a $CoFeS_2$ catalyst, J. Mater. Chem. A, 2022, 10(13), 7048–7057.

11 Z. Hou, X. Zhang, H. Ao, M. Liu, Y. Zhu and Y. Qian, Passivation effect for current collectors enables high-voltage aqueous sodium ion batteries, Mater. Today Energy, 2019, 14, 100337.

12 L. Deng, Y. Zhang, R. Wang, M. Feng, X. Niu, L. Tan and Y. Zhu, Influence of KPF_6 and KFSI on the performance of anode materials for potassium-ion batteries: a case study of MoS_2, ACS Appl. Mater. Interfaces, 2019, 11(25), 22449–22456.

13 N. Fu, Y. T. Xu, S. Zhang, Q. Deng, J. Liu, C. J. Zhou, X. W. Wu, Y. G. Guo and X. Zeng, Electrode materials for aqueous multivalent metal-ion batteries: Current status and future prospect, J. Energy Chem., 2021, 67, 563–584.

14 C. Liu, X. Xie, B. Lu and S. Liang, Electrolyte strategies toward better zinc-ion batteries, ACS Energy Lett., 2021, 6(3), 1015–1033.

15 L. Liu, Y. C. Wu, P. Rozier, P. L. Taberna and P. Simon, Alkali ions pre-intercalated layered MnO_2 nanosheet for zinc-ions storage, Adv. Energy Mater., 2021, 11(31), 2101287.

16 Y. Yang, S. Liang, B. Lu and J. Zhou, Eutectic electrolyte based on N-methylacetamide for highly reversible zinc–iodine battery, Energy Environ. Sci., 2022, 15(3), 1192–1200.

17 S. Qian, J. Zhou, M. Peng, Y. Qian, Y. Meng, Y. Jiang, X. Zeng, J. Liu, T. Qian and C. Yan, A Lewis acidity adjustable organic ammonium cation derived robust protecting shield for stable aqueous zinc-ion batteries by inhibiting the tip effect, Mater. Chem. Front., 2022, 6(7), 901–907.

18 X. Li, Y. Tang, C. Li, H. Lv, H. Fan, W. Wang, T. Cai, Y. Cui, W. Xing and Z. Yan, J. Mater. Chem. A, 2022, 10(9), 4739–4748.

19 D. Chao and H. J. Fan, Intercalation pseudocapacitive behavior powers aqueous batteries, Chem, 2019, 5(6), 1359–1361.

20 W. Du, E. Ang, Y. Yang, Y. Zhang, M. Ye and C. Li, Challenges in the material and structural design of zinc anode towards high-performance aqueous zinc-ion batteries, Energy Environ. Sci., 2020, 13(10), 3330–3360.

21 R. Zhang, S. Wang, S. Chou and H. Jin, Research development on aqueous ammonium-ion batteries, Adv. Funct. Mater., 2022, 32(25), 2112179.

22 C. Wessells, S. Peddada and M. McDowell, The effect of insertion species on nanostructured open framework hexacyanoferrate battery electrodes, J. Electrochem. Soc., 2011, 159(2), A98.

23 X. Wu, Y. Qi, J. Hong, H. Jiang, A. Hernandez and X. Ji, (A03 Best Poster Winner) Ammonium Intercalation Chemistry in Prussian Blue Analogues for, Energy Storage, 2018, 3, 509.

24 C. Li, J. Wu, F. Ma, Y. Chen, L. Fu, Y. Zhu, Y. Zhang, P. Wang, Y. Wu and W. Huang, High-rate and high-voltage aqueous rechargeable zinc ammonium hybrid battery from selective cation intercalation cathode, ACS Appl. Energy Mater., 2019, 2(10), 6984–6989.

25 C. Li, W. Yan, S. Liang, P. Wang, J. Wang, L. Fu, Y. Zhu, Y. Chen, Y. Wu and W. Huang, Achieving a high-performance Prussian blue analogue cathode with an ultra-stable redox reaction for ammonium ion storage, Nanoscale Horiz., 2019, 4(4), 991–998.

26 C. Li, D. Zhang, F. Ma, T. Ma, J. Wang, Y. Chen, Y. Zhu, L. Fu, Y. Wu and W. Huang, A high-rate and long-life aqueous rechargeable ammonium zinc hybrid battery, ChemSusChem, 2019, 12(16), 3732–3736.

27 M. Xia, X. Zhang, H. Yu, Z. Yang, S. Chen, L. Zhang, M. Shui, Y. Xie and J. Shu, Hydrogen bond chemistry in $Fe_4[Fe(CN)_6]_3$ host for aqueous NH_4^+ batteries, Chem. Eng. J., 2021, 421, 127759.

28 X. Wang, Z. Zhang, B. Xi, W. Chen, Y. Jia, J. Feng and S. Xiong, Advances and perspectives of cathode storage chemistry in aqueous zinc-ion batteries, ACS Nano, 2021, 15(6), 9244–9272.

29 Y. Song, Q. Pan, H. Lv, D. Yang, Z. Qin, M. Zhang, X. Sun and X. Liu, Ammonium-ion storage using electrodeposited manganese oxides, Angew. Chem., 2021, 133(11), 5782–5786.

30 D. Yang, Y. Song, M.-Y. Zhang, Z. Qin, J. Liu and X. Liu, Solid–Liquid Interfacial Coordination Chemistry Enables High-Capacity Ammonium Storage in Amorphous Manganese Phosphate, Angew. Chem., 2022, 134(37), e202207711.

31 H. Li, J. Yang, J. Cheng, T. He and B. Wang, Flexible aqueous ammonium-ion full cell with high rate capability and long cycle life, Nano Energy, 2020, 68, 104369.

32 F. Simon, M. J. B, W. Ruocun, Z. Cheng, J. De-En, P. Volker and A. Veronica, Pseudocapacitance: from fundamental understanding to high power energy storage materials, Chem. Rev., 2020, 120(14), 6738–6782.

33 S. Dong, W. Shin, H. Jiang, X. Wu, Z. Li, J. Holoubek, W. F. Stickle, B. Key, C. Liu and J. Lu, Ultra-fast NH_4^+ storage: strong H bonding between NH_4^+ and bi-layered V_2O_5, Chem, 2019, 5(6), 1537–1551.

34 C. Han, J. Zhu, K. Fu, D. Deng, W. Luo and L. Mai, A high-capacity polyaniline-intercalated layered vanadium oxide for aqueous ammonium-ion batteries, Chem. Commun., 2022, 58(6), 791–794.

35 A. Majumdar, G. Scholz and R. Hippler, Structural characterization of amorphous hydrogenated-carbon nitride (aH-CNx) film deposited by CH_4/N_2 dielectric barrier discharge plasma: 13C, 1H solid state NMR, FTIR and elemental analysis, Surf. Coat. Technol., 2009, 203(14), 2013–2016.

36 A. Zecchina, L. Marchese, S. C. P. Bordiga and E. Gianotti, Vibrational spectroscopy of NH_4^+ ions in zeolitic materials: An IR study, J. Phys. Chem. B, 1997, 101(48), 10128–10135.